Three-Dimensional Computational Polarimetric Imaging with a Hyperuniform Frequency-Diverse Metacavity Transceiver

Mengran Zhao, *Member, IEEE*, Shitao Zhu, Xiaoming Chen, *Senior Member, IEEE*, Thomas Fromenteze, Qammer H. Abbasi, *Senior Member, IEEE*, Akram Alomainy, *Senior Member, IEEE*, Vincent Fusco, *Fellow, IEEE*, and Okan Yurduseven, *Senior Member, IEEE*

Abstract—Polarimetric information is beneficial for enhancing the imaging quality of computational imaging systems. However, the hardware that can extract the polarimetric information in a computational polarimetric imaging (CPI) system remains heavily unstudied. Thus, in this paper, a hyperuniform frequency-diverse metacavity transceiver (HFDMT) that is capable of retrieving the polarimetric information throughout the K-band is proposed. The proposed HFDMT is a metacavity etched with cross-shaped irises arranged in a hyperuniform distribution. The transmitter and the receiver of a conventional CPI system are replaced by two isolated ports of the HFDMT, which significantly simplifies the hardware architecture. Firstly, to satisfy the requirements for extracting the polarimetric information while sustaining the high efficiency and the frequency-diversity, the cross-shaped iris is proposed. The cross-shaped iris working efficiently and independently under two orthogonal polarizations also exhibits frequency-diverse radiation responses. Moreover, to improve the spatial-orthogonality of the measurement modes, the hyperuniform distribution is adopted to arrange the irises. Using the hyperuniform distribution results in up to 33% increase in the number of useful measurement modes under different signal-to-noise ratios, as compared to the uniform distribution. Then, the performance of the HFDMT is evaluated. The S-parameters demonstrate that the HFDMT exhibits good impedance match and high port isolation characteristics. In total 600 measurement modes with correlation coefficients lower than 0.35 are obtained from 18 to 26 GHz. Finally, a prototype is fabricated. The 3D CPI feasibility using the proposed HFDMT is verified by both full-wave simulations and measurements.

Index Terms— Hyperuniform; frequency-diverse; metacavity; transceiver; computational polarimetric imaging.

I. INTRODUCTION

COMPUTATIONAL imaging (CI) has gained great traction due to its potential in microwave imaging applications, such as security screening, through-the-wall imaging, autonomous driving, etc. [1-5]. Unlike conventional imaging systems such as the synthetic aperture radar (SAR) or the phased array radar (PAR), no raster scanning mechanism is needed under the CI scheme, which relaxes the hardware constraints and improves the data acquisition efficiency [6-9]. In an ideal CI scenario, the scene is illuminated by a set of orthogonal measurement modes [9] and the target information is compressed into the echoes. The echoes are detected by the receiver, from which the scene is reconstructed by solving an inverse problem [10, 11].

To meet the requirements of CI, various types of metasurface antennas (MAs) that can generate spatially-orthogonal radiated fields have been proposed [9]. According to its working mechanism, the MAs can be divided into the frequency-diverse MA (FDMA) [10-14] and the dynamic MA (DMA) [15-19]. The FDMA can generate diverse radiated fields to encode the scene information by means of a simple frequency sweep, which is commonly realized via metamaterial elements with different resonance features or diverse feeding structures [10, 12]. As for the DMA modalities, spatially varying radiation fields can be obtained not only at different working frequencies, but also under different modulation states [19]. The DMA method offers a greater design flexibility but comes with the cost of increased hardware complexity.

In the conventional CI regime, the information retrieved by the MA only contains the scalar information of the scene, which restricts the quality of the reconstructed image. To improve the imaging quality, an additional set of information, namely the polarimetric information, can be utilized to reveal the target geometrical characteristics [20-22]. This method is called the computational polarimetric imaging (CPI). For a CPI-oriented MA, radiated fields should have two orthogonal polarization states to acquire the polarimetric information. The over-sized cavity-backed FDMA [20, 21] and the two-dimensional DMA [22] have been proposed to validate the feasibility of the MA-based CPI. However, most of these works primarily focus on the theoretical framework of CPI, leaving a significant lack of understanding on the MA design for CPI. In addition, to make CPI a feasible alternative to conventional imaging modalities, new imager topologies improving key system metrics, such as
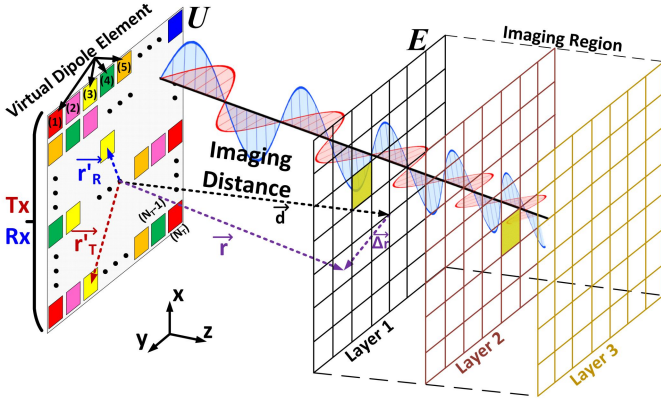
Fig. 1 The architecture of the MA-based 3D CPI.

hardware complexity, practicality and form-factor, are needed.

Aiming to propose a new topology for a CPI-oriented imager, a hyperuniform frequency-diverse metacavity transceiver (HF-DMT) is presented in this paper. The proposed HFDMT is a metacavity [23] etched with cross-shaped irises arranged in a hyperuniform distribution. The hyperuniform distribution is an array unit distribution way evolving through natural selection, which is a disordered solution to the array design [24, 25]. The hyperuniform distribution can increase the randomness, which is validated in radar cross section (RCS) reduction applications [26]. The frequency-diversity of the proposed new topology is improved by using the random metasurface, the cross-shaped iris, and the hyperuniform distribution. Moreover, to simplify the architecture, the transmitter and the receiver are replaced by the two ports of the HFDMT, multiplexing the same aperture. The proposed HFDMT topology addresses the challenge of balancing hardware complexity, integrability and practicality, offering a promising hardware solution for CPI applications.

The rest of this paper is organized as follows. In Section II, the HFDMT-based CPI process is introduced, which specifies the hardware requirements. In Section III, the HFDMT design is introduced in detail. Firstly, a random metasurface providing varying reflection responses at different frequencies and under orthogonal polarization states is designed. Then, a cross-shaped iris exhibiting diverse radiation characteristics both at different working frequencies and under orthogonal polarization states is proposed. Finally, the hyperuniform distribution is utilized to arrange the designed irises. In Section IV, the performance of the proposed HFDMT is evaluated, including the reflection coefficients (S$_{11}$ and S$_{22}$), the transmission coefficient (S$_{21}$), the singular values (SVs) and the correlation coefficients (CCs) of measurement modes. In total 600 measurement modes with CCs lower than 0.35 are obtained from 18 to 26 GHz. In Section V, the CPI simulations and experiments are carried out and the target images are reconstructed in a three-dimensional (3D) imaging region under different conditions. In Section VI, the paper is concluded.

II. COMPUTATIONAL POLARIMETRIC IMAGING

In a MA-based CPI system, as shown in Fig. 1, the electric field (E) radiated by the transmitter (Tx) is used to illuminate the imaging region and the scattered field is captured by the
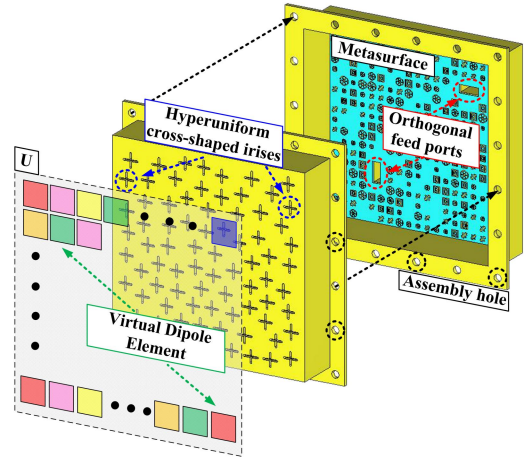

Fig. 2 Schematic diagram of the proposed HFDMT.

receiver (Rx) [22]. Following the first Born approximation [27], the detected signal can be expressed as:

$$g(f_i) = \sum_{i=1}^{M} \sum_{j=1}^{Q} \boldsymbol{E}_T(r_j, f_i)\overline{\chi}(r_j)\boldsymbol{E}_R(r_j, f_i)^T \qquad (1)$$

where M and Q refer to the number of working frequencies and scene voxels. $\boldsymbol{E}(\boldsymbol{r}, f)$ denotes radiated fields propagated to the imaging region. $[\cdot]^T$ is the transpose operation. $\overline{\chi}(\boldsymbol{r})$ represents the susceptibility tensor, which is a 3×3 matrix containing all the interaction information between the $\boldsymbol{E}_T$ and the $\boldsymbol{E}_R$ over the imaging region [20].

The radiated fields can be calculated through the near-field to far-field transformation $\boldsymbol{E}(\boldsymbol{r}, f) = \boldsymbol{U}(\boldsymbol{r}', f)G(\boldsymbol{r}', \boldsymbol{r}, f)$ [28, 29]. As shown in Fig. 1, $\boldsymbol{U}$ is a 3×1 vector ($[U^x; U^y; U^z]$) denoting the 3D aperture field, $\boldsymbol{r}'$ refers to the position vector of a virtual dipole element (i.e., magnetic dipole calculated from $\boldsymbol{U}$ [29]), and $\boldsymbol{r}$ represents the position vector from the origin to a voxel in the imaging region [21]. $G(\boldsymbol{r}', \boldsymbol{r}, f)$ is the Green's function.

For simplification, (1) can be written into a matrix form as:

$$\begin{bmatrix} g(f_1) \\ g(f_2) \\ \vdots \\ g(f_M) \end{bmatrix} = \begin{bmatrix} \overline{H}(f_1, p_1) & \overline{H}(f_1, p_2) & \cdots & \overline{H}(f_1, p_Q) \\ \overline{H}(f_2, p_1) & \overline{H}(f_2, p_2) & \cdots & \overline{H}(f_2, p_Q) \\ \vdots & \vdots & \ddots & \vdots \\ \overline{H}(f_M, p_1) & \overline{H}(f_M, p_2) & \cdots & \overline{H}(f_M, p_Q) \end{bmatrix} \begin{bmatrix} \overline{\chi}(p_1) \\ \overline{\chi}(p_2) \\ \vdots \\ \overline{\chi}(p_Q) \end{bmatrix} \quad (2)$$

where $g(f_M)$ refers to the detected signal at frequency f_M, $\overline{H} \propto \boldsymbol{E}_T \boldsymbol{E}_R^T$ is the measurement mode matrix and $\overline{\chi}(p_Q)$ denotes the susceptibility tensor of the Q_{th} scene voxel. To ensure that all detections are effective, the $\boldsymbol{E}$ should ideally be of the same amplitude level. This would ensure that the measured signal $\boldsymbol{g}$ can fully benefit from the orthogonality of the $\overline{H}$ when all detections exhibit similar response amplitudes. By employing the least-squares (LS) algorithm to solve an ill-conditioned inverse problem, the target image for CPI can be reconstructed on nine polarization bases (χ_{ij}, where $i, j = x, y, z$) [20-22].

Although the MA-based CPI is simpler than the array-based CPI, at least one Tx and one Rx are still required, which puts a burden on the system calibration [3, 9, 20, 30]. Thus, for further simplification, the HFDMT multiplexing the aperture as shown in Fig. 2 is proposed in this paper. Because the radiated field

patterns would be different when fed by different ports [31, 32], two orthogonal feed ports are used to replace the Tx and the Rx as shown in Fig. 2. In this architecture, the Tx and the Rx are merged into the HFDMT while maintaining the low-correlated measurement modes, which means the HFDMT can share the same CPI algorithm with the MA. Nevertheless, the integration also introduces new requirements on the port isolation and the disparity between orthogonal-polarized measurement modes at the same frequency, which should be considered in the imager design.

III. DESIGN OF THE HFDMT

According to the aforementioned analysis, the imager should be capable of generating spatially-orthogonal radiated fields at different frequencies, under orthogonal polarizations as well as when excited through different ports. Moreover, the isolation of different ports should be high enough to avoid the interference. Hence, the HFDMT shown in Fig. 2 is proposed.

The proposed HFDMT is a compact metacavity etched with different cross-shaped irises in a hyperuniform distribution. A metasurface with high-dispersion characteristics is placed on the bottom of the metacavity to realize the frequency-diversity.

Owing to the adoption of frequency-diverse metasurface and the hyperuniform distribution, the HFDMT can generate 600 measurement modes within the working bandwidth, which is creditable considering its limited size [33].

A. Design of the Frequency-Diverse Metacavity

The 3D aperture field of a metacavity-backed imager can be expressed as:

$$U(r_n', f) = \sum_{n=1}^{N} A_n(r_n', f)\, I(r_n', f) \qquad (3)$$

where $A_n(r_n', f)$, referred to as the radiation vector (RV), represents the modulation introduced by the n_{th} radiating iris locating at r_n'. $I_n(r_n', f)$, referred to as the excitation vector (EV), denotes the source filed projected onto the top surface of the metacavity. In order to generate different radiated fields at different frequencies, the RV and/or the EV should vary with the frequency. In this paper, the RV and the EV are provided by the cross-shaped iris and the metacavity, respectively.

Here, we firstly focus on achieving frequency-diverse EVs. In our previous work [20, 21], an electrically over-sized cavity with a size of $21\lambda \times 21\lambda \times 11\lambda$ (λ is the free-space wavelength at its central frequency 24 GHz) has been proven qualified for this purpose. The EV diversity of an electrically over-sized cavity is from the modulation of random irregular structures in the cavity. The irregular and convex boundaries can induce the degeneration of the inherent resonant modes, thereby achieving different EVs at different working frequencies [20]. However, the performance of this method is closely tied to the cavity size. In other words, if the cavity size is limited, the number of useful measurement modes would significantly decrease. To address this challenge, an alternative metacavity architecture exhibiting competitive frequency-diversity with a compact size has been proposed in [23]. By employing a high-dispersion random metasurface, the EV of a metacavity would vary with the
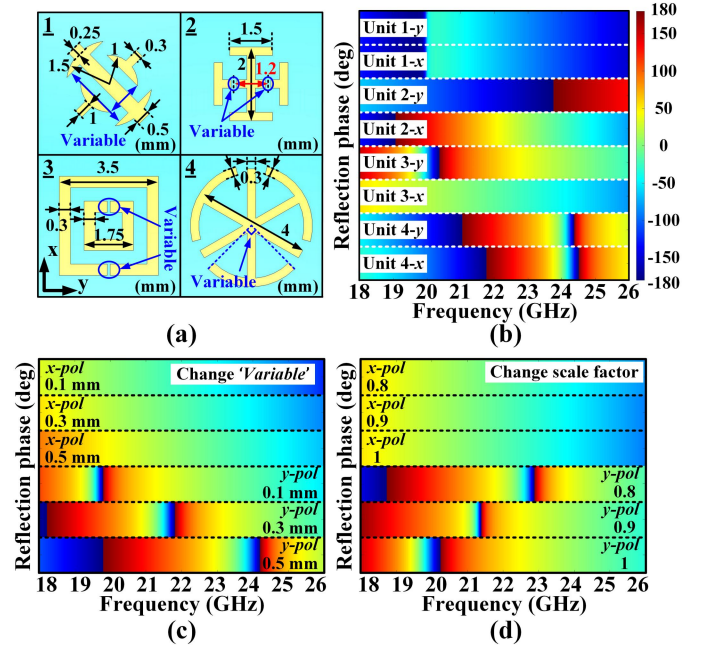

Fig. 3 Basis metamaterial elements across the random metasurface. (a) Element topologies with dimensions; (b) Reflection phases of each element under orthogonal polarization states; Reflection phases when changing (c) the structural parameter, and (d) the scale factor.

operating frequency. However, the requirements of different reflection responses under different polarization states were not considered in [23]. Furthermore, the radiation iris topology in [23] is not suitable for CPI due to the unevenness of radiated fields under different polarization states. Therefore, regarding the CPI requirements, the metacavity in this work is totally different from that in [23].

In this paper, a size-limited ($8\lambda \times 8\lambda \times 4\lambda$) metacavity is proposed to achieve the frequency-diverse EVs. Additionally, in view of the requirement on the difference between radiated fields under different polarizations, the metacavity should also exhibit dual-polarized radiation characteristics, constituting a new requirement on the metacavity architecture. In summary, the random metasurface, as the vital part of the metacavity, should exhibit different responses at different frequencies as well as under different polarizations.

Consequently, four kinds of metamaterial elements as shown in Fig. 3(a) are used as the basis elements to design the random metasurface. Following the metacavity design principle in [23], the reflection responses of these metamaterial elements should be different at different frequencies. Moreover, considering the dual-polarization requirement of CPI, each element should also have different reflection responses under different polarizations. The reflection phases of four basis metamaterial elements are shown in Fig. 3(b). It is evident that each element has its own frequency-polarization-diverse reflection phase. Furthermore, the reflection response of the same kind of element can also be altered by changing the structural parameters (i.e., 'Variable' in Fig. 3(a)) or assigning different scale factors [23, 34]. Here, as an example, and without loss of generality, we can consider the element 3. As shown in Fig. 3(c), when changing the gap width (see 'Variable' in Fig. 3(a)) from 0.1 to 0.5 mm, the reflection phases are altered. Likewise, when assigning different scale
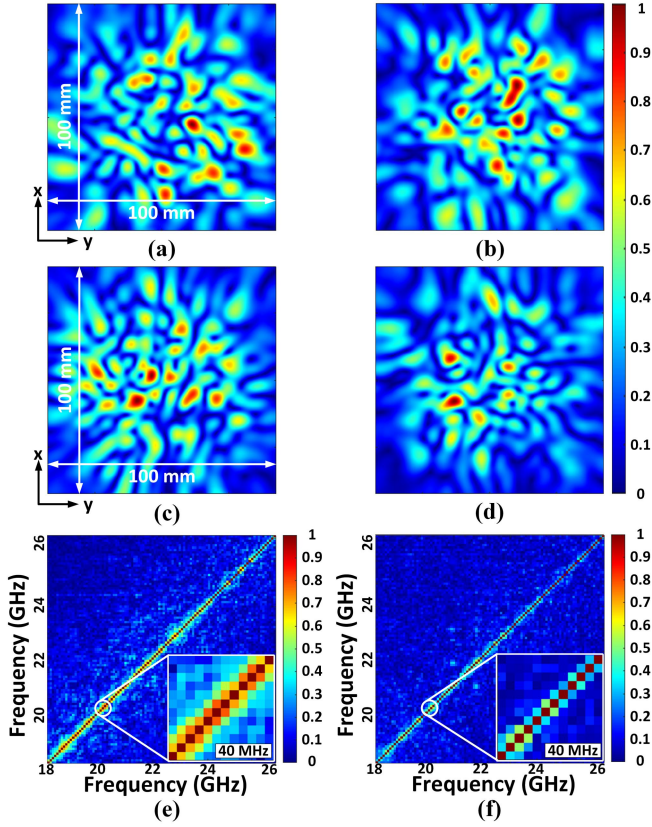
Fig. 4 Normalized reflected electric fields of the random metasurface at 22 GHz under (a) x-polarization, (b) y-polarization; at 22.05 GHz under (c) x-polarization, (d) y-polarization; The CCs of the radiated fields of the HFDMT (e) without the random metasurface; (f) with the random metasurface.
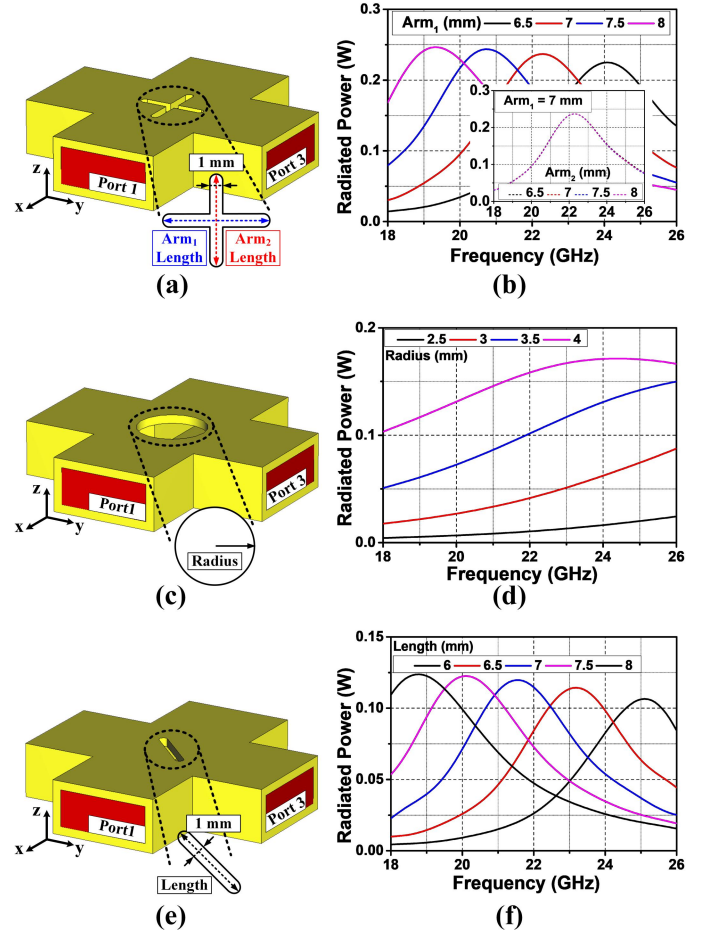

Fig. 5 (a) Schematic and (b) radiated power of the cross-shaped iris; (c) Schematic and (d) radiated power of the circular iris; (e) Schematic and (f) radiated power of the slot iris.

factors to the element, as shown in Fig. 3(d), the reflection phases are also changed. Finally, the random metasurface is achieved by randomly placing different kinds of metamaterial elements with different structural para- meters and scale factors over the aperture.

The reflected electric fields of the random metasurface are shown in Fig. 4. From Figs. 4(a) and 4(b), we can conclude that the random metasurface exhibits different reflection responses under different polarization states. Figs. 4(a) and 4(c) prove that the reflection response of the random metasurface also varies with the operating frequency. In order to validate the advantage of loading the HFDMT with the random metasurface, the CCs of the HFDMT radiated fields with and without the random metasurface are evaluated. From the comparison between the Figs. 4(e) and 4(f), it is evident that the CCs of radiated fields at adjacent working frequencies are significantly decreased after loading the HFDMT with the random metasurface.

In conclusion, loading the HFDMT with the random metasurface plays a crucial role in enabling the metacavity to provide varying EVs at different frequencies, laying a foundation for generating frequency-diverse radiated fields.

As for the feeding structure, high isolation of two feed ports is required to avoid the interference. Therefore, two orthogonal standard WR42 waveguide ports are utilized as shown in Fig. 2, whose inner cross section is 10.668 mm×4.318 mm. The size of the metacavity is 100 mm × 100 mm × 50 mm ($8\lambda \times 8\lambda \times 4\lambda$).

B. Design of the Cross-Shaped Iris

According to (3), another factor that influences the aperture field U is RV. In order to provide frequency-diverse RVs, the iris should exhibit different radiation characteristics at different frequencies. Besides, taking into account the dual-polarization requirement, the iris should be able work independently under different polarization states. A four-port waveguide structure as shown in Fig. 5 is used as the excitation to evaluate the irises. The center-etched iris would work under different polarization states when it is fed through port 1 or port 3, respectively. To ensure a fair assessment of different irises, the input power is standardized at 0.5 W.

Considering the aforementioned analyses, a cross-shaped iris as shown in Fig. 5(a) is proposed. The cross-shaped iris consists of two perpendicular arms with different lengths. As shown in Fig. 5(b), when feeding through port 1, the frequency at which the highest radiated power occurs varies as a function of the length of Arm_1 (see in Fig. 5(a)), while changing the length of Arm_2 does not affect the radiation response in this polarization basis. Due to the symmetry of the cross-shaped iris, similar phenomena can be observed when feeding through port 3. It can be seen from the analysis shown in Fig. 5(b) that the maximum radiated power is 0.25 W. From Fig. 5(b), we can conclude that the cross-shaped iris is able to offer different RVs at different
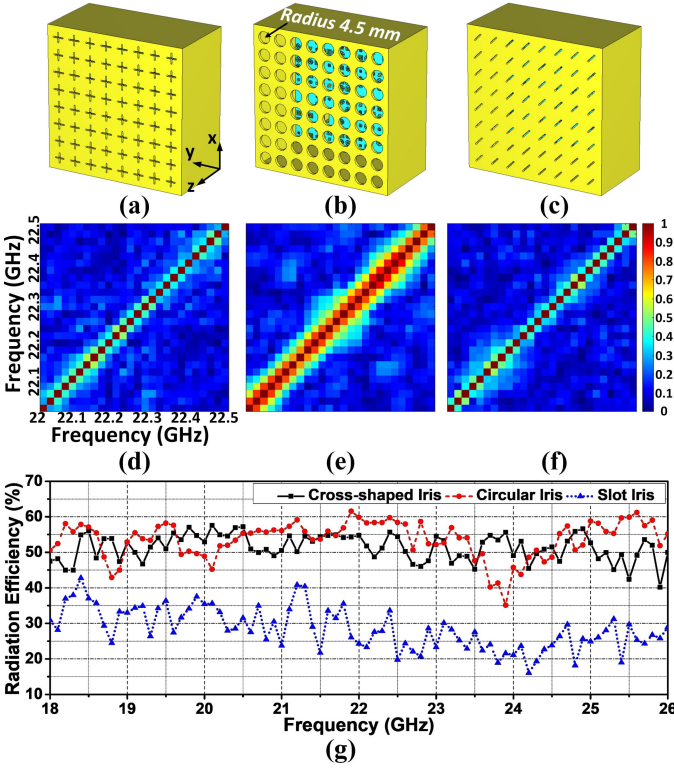
Fig. 6 Layout of the (a) cross-shaped iris-based, (b) circular iris-based, and (c) slot iris-based UFDMTs; CCs of the radiated fields generated by the (d) cross-shaped iris-based, (e) circular iris-based, and (f) slot iris-based UFDMTs; (g) Radiation efficiencies of the three UFDMTs.

frequencies and under different polarizations when the length of Arm_1 and Arm_2 are controlled independently. Consequently, if different lengths are randomly assigned to different irises, the RVs would be frequency-diverse under two polarization states. To ensure that the radiated fields at each frequency are of the same level, the arm length is chosen with equal probability from 6.5 to 8.5 mm.

Compared to our previous iris designs, such as the circular iris [20] shown in Fig. 5(c) and the slot iris [23] shown in Fig. 5(e), the cross-shaped iris is more suitable for CPI applications. As shown in Fig. 5(d), the circular iris can radiate uniformly within the operating bandwidth. However, the circular iris has similar radiation performance at different working frequencies. Hence, the frequency-diversity of a circular iris-based cavity imager only relies on the EV, which results in the reduction of frequency-diversity. As for the slot iris shown in Fig. 5(e), it is rotated by 45° for the dual-polarized radiation. Though the slot iris exhibits the frequency-diverse characteristic, its radiated power, as shown in Fig. 5(f), is lower than the cross-shaped iris.

To prove the advantage of the cross-shaped iris, as shown in Fig. 6, three uniform frequency-diverse metacavity transceivers (UFDMTs) are modeled in CST Microwave Studio. The only difference among the three UFDMTs lies in the structure of the iris. From Figs. 6(d), 6(e) and 6(f), it is evident that the CCs of the radiated fields generated by the circular iris-based UFDMT are higher than those of the radiated fields generated by the cross-shaped iris-based and the slot iris-based ones at adjacent frequencies. The comparison proves that the cross-shaped iris-based and the slot iris-based UFDMTs have better
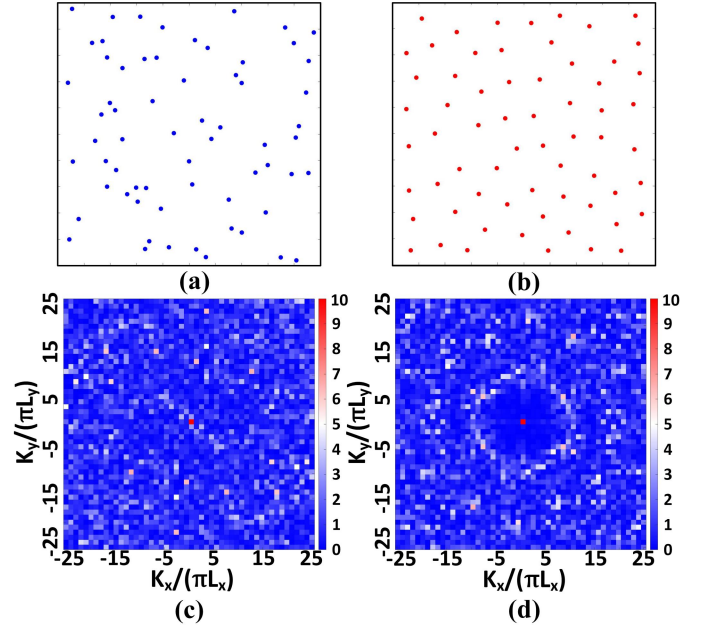

Fig. 7 (a) The random distribution; (b) The hyperuniform distribution; Structure factors of the (c) random distribution and (d) hyperuniform distribution.

frequency-diversity, which is in consistent with the analyses of irises in Fig. 5. The simulated radiation efficiencies of three UFDMTs are shown in Fig. 6(g). The radiation efficiencies of the cross-shaped iris-based and the circular iris-based UFDMTs are markedly higher than the slot iris-based one. From Fig. 6(g), the radiation efficiencies of the cross-shaped iris-based and the circular iris-based UFDMTs are comparable. This is because the cross-shaped iris radiates less efficiently outside its designated working frequencies (see Fig. 5(b)), whereas the circular iris maintains similar radiation performance across a broadband range consistently (see Fig. 5(d)). Therefore, from the aperture synthesis, the radiation efficiencies of the two cases are similar.

In conclusion, considering both the frequency-diversity and the radiation efficiency, the cross-shaped iris exhibits the best performance and it is finally adopted in this paper.

C. Hyperuniform Distribution

The iris positions, r_n' in (3), also influence the synthesis of the aperture field U. However, there is limited state-of-the-art research on improving the diversity through the iris distribution. Therefore, the hyperuniform distribution is studied and adopted to improve the performance of the HFDMT.

The concept of "hyperuniform" is used to describe a random point distribution in d-dimensional Euclidean space $\mathbb{R}^d$, whose number variance $\sigma_N^2(R)$ within a spherical sampling window of radius R increases at a rate slower than the window volume, i.e., R^d [25, 26, 35, 36]. In Fourier space, hyperuniformity means that the structure factor $S(k)$ will vanish when $|k|$ approaches zero [36], that is:

$$\lim_{|k|\to 0} S(k) = 0 \tag{4}$$

The structure factor $S(k)$ for a N points configuration can be obtained directly from the point positions $r_1, r_2, \cdots, r_N$ as:
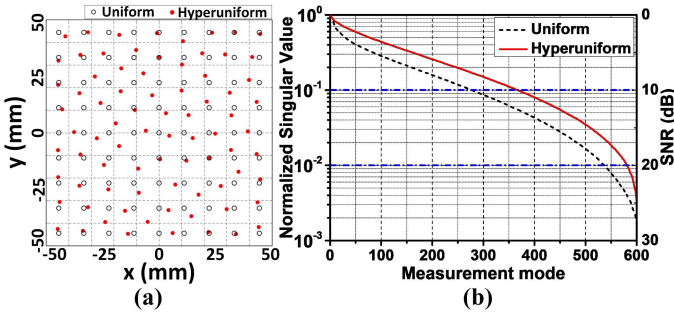
Fig. 8 (a) Uniform distribution and hyperuniform distribution; (b) The normalized singular values of measurement modes generated under the uniform distribution and the hyperuniform distribution.

$$S(\boldsymbol{k}) = \frac{1}{N}\left|\sum_{i=1}^{N} e^{j\boldsymbol{k}\cdot r_i}\right|^2 \qquad (5)$$

where N is the total number of points (under periodic boundary conditions), $\boldsymbol{k}$ is the wave vector associated with the system and boundary conditions.

From the sketch map of HFDMT in Fig. 2, the cross-shaped irises are arranged over the two-dimensional (2D) aperture. So only the 2D hyperuniform distribution is applied in this paper. In this case, $k = (2\pi n_x/L_x, 2\pi n_y/L_y)$, where $n_x, n_y \in \mathbb{Z}$, L_x, L_y are the side lengths of the distribution area. The hyperuniform distribution can be generated through the collective coordinate approach [37-40]. Fig. 7 presents the random distribution and the hyperuniform distribution and their corresponding structure factors. It is hard to discern the hyperuniformity from the point distributions, however, the structure factors are dramatically different. Therefore, the structure factor is preferred to describe the hyperuniform distribution [25, 36].

To describe the degree of the point distribution randomness, the constraint factor $\kappa = M(K)/2N$ is introduced, which is the ratio of the constrained degrees of freedom to the total number of degrees of freedom [36]. The larger the κ value is, the more uniform the point distribution is [39]. Generally, if $\kappa \leq 0.5$, the point distribution belongs to the disordered regime. However, this threshold changes depending on the number of points [36].

In this paper, an 81-point hyperuniform distribution with the constraint factor $\kappa = 0.494$ is generated as shown in Fig. 8(a). In order to demonstrate the performance improvement achieved by adopting the hyperuniform distribution, the normalized SVs of the measurement modes generated by the UFDMT (uniform distribution) and the HFDMT (hyperuniform distribution) are evaluated in Fig. 8(b). The SV curve is used to evaluate the spatial-orthogonality of the measurement modes from a signal processing aspect [41]. A SV curve exhibiting a flat response suggests the spatial-orthogonality of the measurement modes [41]. In other words, it is desired that the SV curves in Fig. 8(b) have a flatter response to maximize the orthogonality of the measurement modes. In view of this, it is evident from Fig. 8(b) that the quality of the measurement modes generated under the hyperuniform distribution is significantly improved compared to those generated under the uniform distribution. A quantitative assessment of Fig. 8(b) reveals that the number of useful measurement modes generated under the hyperuniform distribution is increased by up to 33% under different signal-to-noise
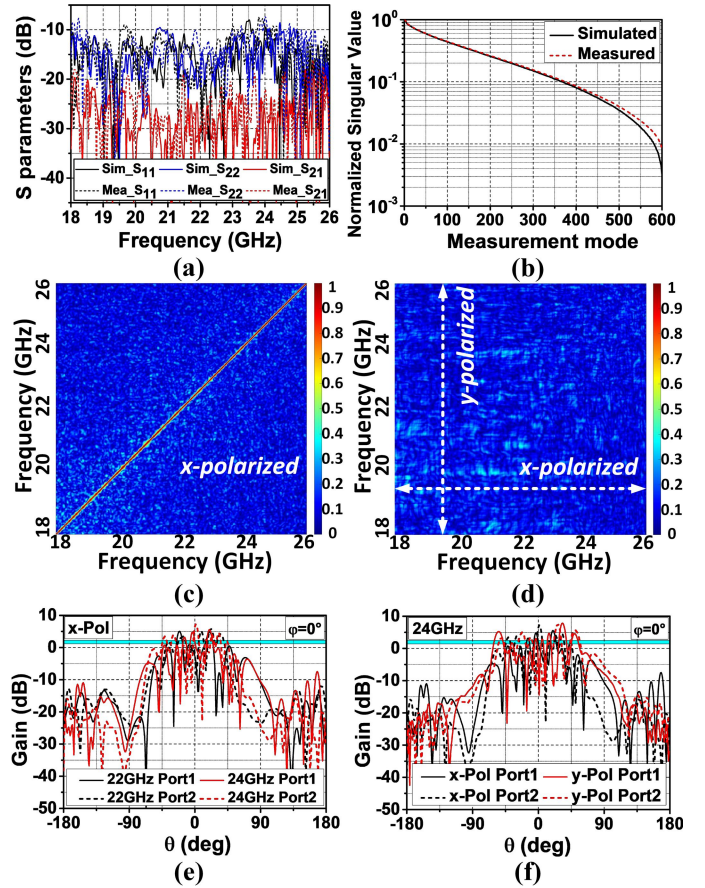

Fig. 9 (a) S parameters; (b) SVs of the measurement modes; Measured CCs (c) at different frequencies and (d) under orthogonal polarization states; Simulated radiation patterns (e) at different frequencies and (f) under orthogonal polarization states.

ratios (SNRs) compared to the uniform distribution. In particular, the numbers of useful measurement modes are increased by 32.85% and 10.28% when the SNRs are 10 dB and 20 dB, respectively. In the context of this analysis, the useful measurement modes are defined as the modes that remain above the system SNR level [11].

In summary, the performance of a metacavity-based imager would be influenced by the EV, the RV, and the iris distribution. By utilizing the random metasurface, the cross-shaped iris, and the hyperuniform distribution, the HFDMT is achieved.

IV. SIMULATIONS AND MEASUREMENTS

In this section, the performance of the proposed HFDMT is evaluated. As shown in Fig. 9(a), the reflection coefficients of the orthogonal feed ports (i.e., S_{11} and S_{22}) are around or under -10 dB within the operating bandwidth, which means the HFDMT has a good impedance-matching response at its input ports. Besides, the transmission coefficients (i.e., S_{21}) between two feed ports are around or under -20 dB across the entire bandwidth, which verifies the high isolation between the two ports. The SV curves shown in Fig. 9(b) exhibit a good agreement between the simulated and the measured results. The CCs of the measurement modes at different frequencies, as shown in Fig. 9(c), are lower than 0.35, demonstrating the frequency-diversity. Moreover, as shown in Fig. 9(d), the CCs
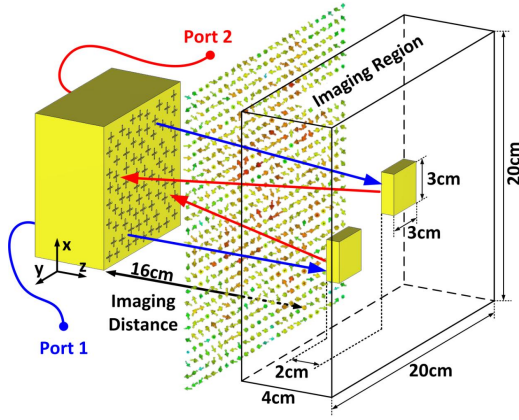
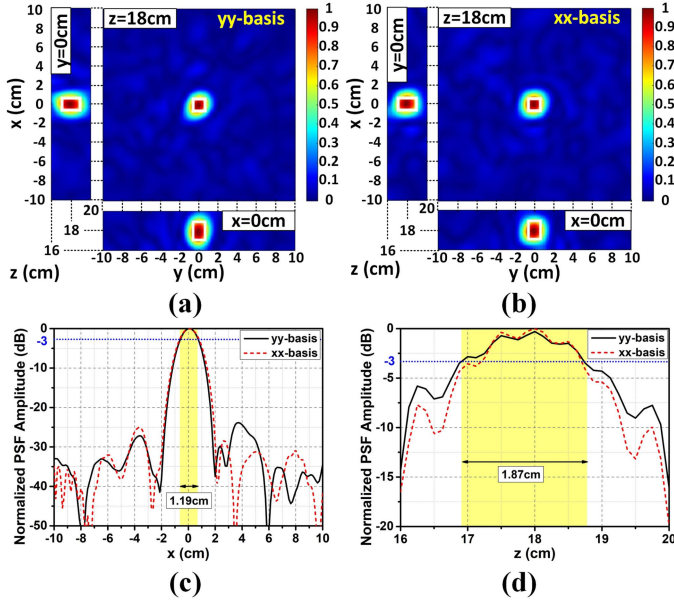Fig. 10 Configuration of the HFDMT-based 3D CPI.

Fig. 11 Reconstructed PSF patterns under (a) the yy-basis and (b) the xx-basis. The PSF curves along (c) the x-axis (cross-range axis) and (d) the z-axis (range axis).

of measurement modes under two orthogonal polarizations are lower than 0.26, validating their differences under different polarizations. Furthermore, to verify that the radiated fields are of the similar amplitude level under different conditions (i.e., frequency, polarization, and feed port), the φ = 0° slice of the simulated radiation patterns at different frequencies and under different polarization states are shown in Figs. 9(e) and 9(f). Figs. 9(e) and 9(f) show that all the radiation patterns are fluctuating at the same level. The difference in the fluctuations proves the diversity of measurement modes, which is important for the CPI imager.

In conclusion, according to the simulated and the measured results, the designed HFDMT is well-fed and a high-isolation between two ports is achieved within the working bandwidth. The SV pattern becomes flatter by adopting the hyperuniform distribution, proving the spatial-orthogonality improvement of the measurement modes. The CCs of 600 measurement modes are lower than 0.35, sufficient for CPI [20-22].

V. 3D IMAGING SIMULATION AND EXPERIMENT

In order to validate the feasibility of the proposed HFDMT, the CPI simulations and experiments are implemented in this section. As depicted in Fig. 10, port 1 and port 2 of the HFDMT are used as the transmitting and receiving port, respectively. The imaging distance is 16 cm and the imaging region is 20 cm×20 cm×4 cm in the x-, y-, and z-direction. The theoretical cross-range (xy-plane) resolution is 1.13 cm at 18 cm, and the theoretical range (z-axis) resolution is 1.875 cm following their definitions given as:

$$\delta_{cr} = \frac{L\lambda_0}{2D} \tag{6}$$

$$\delta_r = \frac{c}{2B} \tag{7}$$

where L is the imaging distance, D is the aperture size, λ_0 is the free space wavelength at the central frequency, c is the speed of light and B is the working bandwidth.

The point spread function (PSF) patterns are analyzed to validate the resolution [42]. As shown in Figs. 11(a) and 11(b), the PSF patterns are reconstructed under different polarization bases. The PSF curves are also presented for the cross-range and the range in Figs. 11(c) and 11(d). From Fig. 11, the simulated cross-range and range resolutions are 1.19 cm and 1.87 cm, confirming the above theoretical calculations.

A. 3D Imaging through CST Simulations

Following the characterization of the resolution limits, we firstly study the 3D CPI concept in CST. The full-wave CST simulation-based 3D imaging is divided into three steps as:

Step 1: Set the E-field monitors at the near-field region of the HFDMT from 18 to 26 GHz with a step width of 10 MHz. The obtained E-field data are the aperture fields (U). Utilizing the near-field to far-field transformation [29], the radiated fields at the imaging region (E) can be calculated. Alternatively, we can directly set the E-field monitors at the imaging region to acquire the radiated fields (E). However, this will occupy more calculation resources and take longer time.

Step 2: Run the simulation without any targets, and acquire the transmission coefficient (S'_{21}) that contains all information of the background.

Step 3: Run the simulations with the target, and acquire the transmission coefficient (S_{21}) containing both the background and the target information. The detected signal g in (2) can be calculated by subtracting S'_{21} from S_{21}. That is $g = S_{21} - S'_{21}$. Then, according to the analysis in Section II, the target image can be reconstructed.

Following the aforementioned process, as shown in Fig. 10, the 3D imaging simulation is carried out in CST. Two identical square patch targets with a side length of 3 cm are placed in the imaging region without overlap. The imaging distances of the two targets in the xy-plane are 17 cm and 19 cm, respectively. The imaging region is divided into 2205 (21×21×5 in x-, y-and z-direction) imaging voxels with the side length of 1 cm, which is selected in accordance with the calculated δ_{cr} in (6). The imaging simulations are implemented using the UFDMT
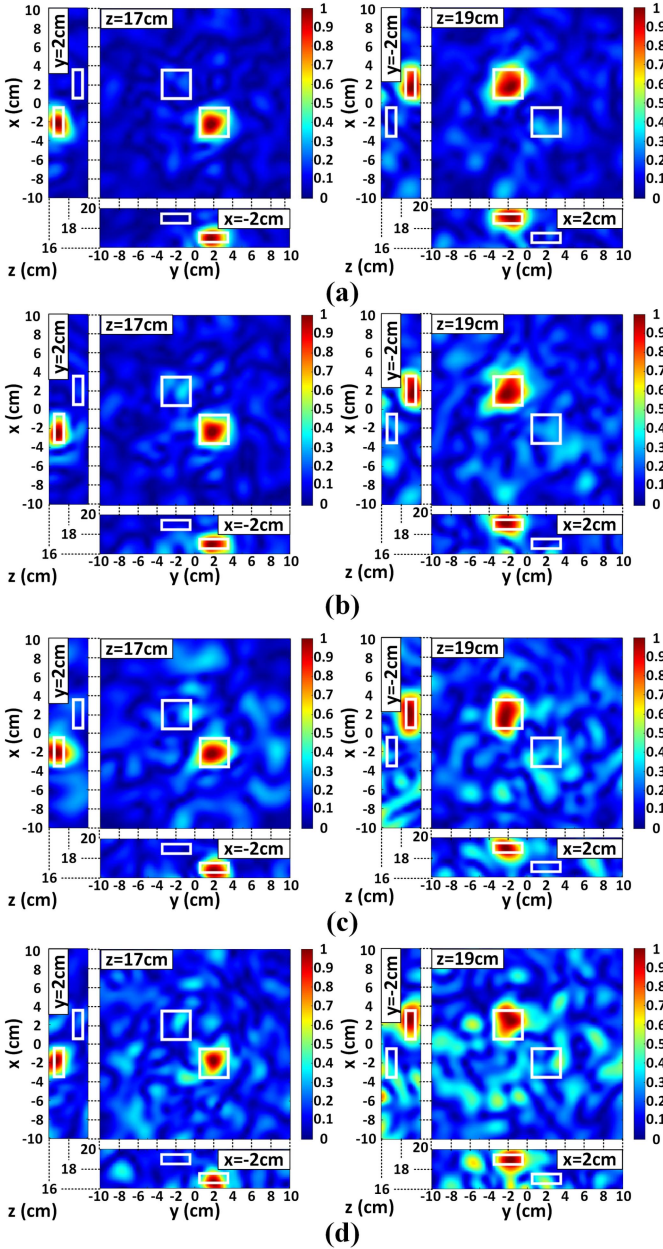
(a)

(b)

(c)

(d)

Fig. 12 Reconstructed images of the 3D imaging in CST simulations. Under 20 dB SNR using the (a) HFDMT and the (b) UFDMT; Under 10 dB SNR using the (c) HFDMT and the (d) UFDMT.

and the HFDMT, respectively. The only difference between two modalities lies in the iris distribution. From the evaluation of SVs shown in Fig. 8(b), the measurement mode quality of the HFDMT is better than that of the UFDMT. The simulations are carried out under different SNRs to prove the performance improvement resulting from the hyperuniform distribution. As shown in Figs. 12 (a) and 12(b), when the SNR is 20 dB, both the HFDMT and the UFDMT can reconstruct two targets with high quality. However, when the SNR decreases to 10 dB, the HFDMT can achieve better imaging quality than the UFDMT as shown in Figs. 12 (c) and 12(d). This is because when the SNR decreases from 20 dB to 10 dB, as shown in Fig. 8(b), the number of useful measurement modes of the HFDMT reduces from 590 to 368, and the number of useful measurement modes of the UFDMT reduces from 535 to 277. Due to a significant
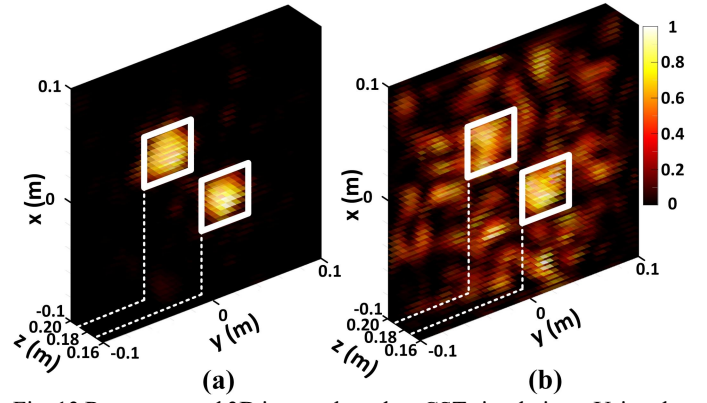

(a)   **(b)**

Fig. 13 Reconstructed 3D images based on CST simulations. Using the HFDMT (a) with the random metasurface and (b) without the random metasurface.

drop in the number of useful measurement modes, the UFDMT imaging quality decreases in Fig. 12. This study confirms the performance improvement offered by the proposed hyperuniform distribution of the HFDMT architecture.

Following the confirmation of the hyperuniform impact for imaging, next, we investigate the effect of loading the HFDMT with the random metasurface. According to the CCs shown in Figs. 4(e) and 4(f), the HFDMT with the random metasurface exhibits lower CCs than the HFDMT without the random metasurface. That is, by loading the random metasurface, more low-correlated measurement modes can be acquired. Hence, to verify the performance improvement, the imaging simulations are carried out using the HFDMT with and without the random metasurface, respectively. The corresponding results are shown in Figs. 13(a) and 13(b). It is evident that the HFDMT with the random metasurface achieves better imaging performance.

B. 3D Imaging through Experiments

As shown in Fig. 14(a), a prototype of the designed HFDMT is fabricated and implemented in the imaging experiments. The experiments are conducted with a SNR of 20 dB. Alongside the square patch targets, a bar target (9 cm×3 cm) is also employed to verify the CPI feasibility of the HFDMT and it is placed at a distance of 20 cm in the imaging region. The used bar target is polarization sensitive due to its large aspect ratio.

The imaging experiment is divided into two steps:

Step 1: Near-field scan. A probe is placed 10 cm opposite the HFDMT to measure the x- and y-polarized electric-field. The scanning region is 20 cm×20 cm with a step width of 0.5 cm. The aperture fields generated when feeding through port 1 and port 2 are measured individually, and from these measurements, the E_T and the E_R are calculated [28].

Step 2: Signal measurement. The HFDMT and the targets are placed as depicted in Fig. 14 (a). The transmission coefficients (S_{21}) of the HFDMT are measured separately, both without and with the target. Then the detected signal g can be calculated. Ultimately, the target image is reconstructed as analyzed above.

The imaging results of two square patch targets are shown in Figs. 14(b) and 14(c). It is evident that the imaged square patch targets are clearly identified in two depth slices (z =17 cm and z = 19 cm), which experimentally validates the 3D imaging capability of the HFDMT.
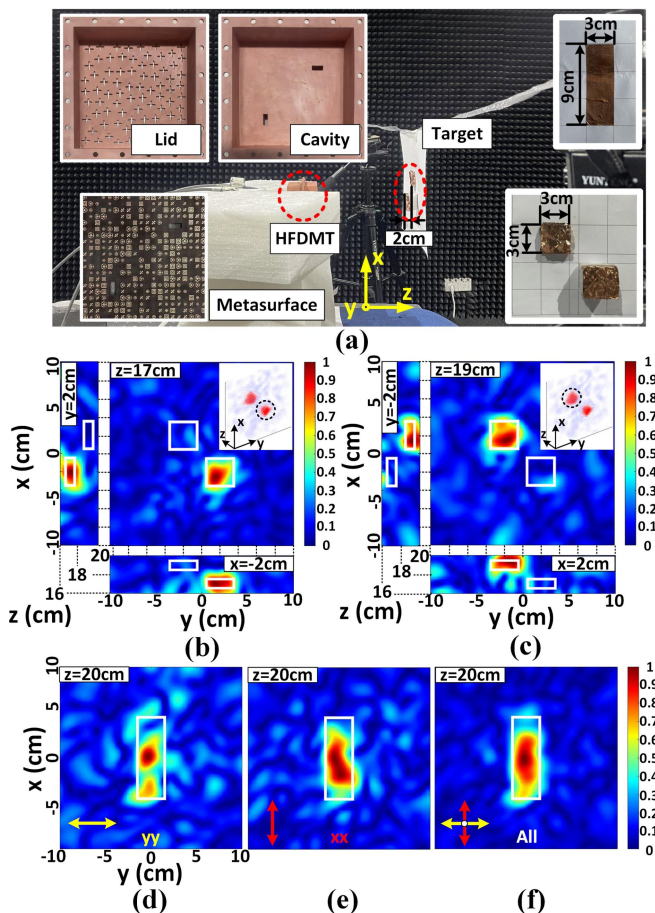
Fig. 14 (a) Real scene of the HFDMT-based 3D CPI experiment; Images reconstructed under 20 dB SNR of (b) the ahead square patch target; (c) the behind square patch target; The imaged bar target under (d) the yy-basis, (e) the xx-basis, and (f) all-bases.

Analyzing the imaging results shown in Figs. 14(d) and 14(e), we can conclude that the quality of the imaged bar target varies under different polarization basis. That is, the bar target is not well-imaged under the yy-basis. However, the imaging quality under the xx-basis is significantly improved. Figs. 14(d), 14(e) and 14(f) prove the advantage of the CPI method in offering the capability to probe polarization-dependent target information as a function of different polarization bases [20-22, 43].

VI. Conclusion

In this paper, a HFDMT-based CPI system was proposed, in which the Tx and the Rx were replaced by two isolated ports. Firstly, the HFDMT was achieved by a metacavity etched with cross-shaped irises in a hyperuniform distribution. By utilizing the random metasurface, the cross-shaped iris, as well as the hyperuniform distribution, the spatial-orthogonality of the measurement modes was significantly improved. Measurement modes are spatially-orthogonal both at different frequencies and under different polarization states. Then, the performance of the proposed HFDMT was evaluated. From the S_{11}, S_{22} and S_{21}, the designed HFDMT exhibits good impedance match and high port isolation characteristics across the K-band. In total 600 measurement modes with CCs lower than 0.35 were obtained from 18 to 26 GHz. Finally, the 3D CPI feasibility of the HFDMT was validated by simulations and experiments. Two spatially non-overlapped square patch targets were used to demonstrate the 3D imaging capability and a polarimetric bar target was used to validate the CPI performance. The proposed HFDMT-based CPI method is simple in architecture. However, it still remains a challenge to improve the isolation between two feed ports in order to increase the imaging distance.

References

[1] D. M. Sheen, D. L. Mcmakin, and T. E. Hall, " Three-dimensional millimeter-wave imaging for concealed weapon detection," *IEEE Trans. Microw. Theory Techn.*, vol. 49, no. 9, pp. 1581-1592, Sept. 2001.

[2] M. Elsdon, O. Yurduseven, and D. R. Smith, "Early stage breast cancer detection using indirect microwave holography," *Prog. Electromagn. Res.*, vol. 143, pp. 405-419, 2013.

[3] O. Yurduseven, J. N. Gollub, A. Rose, D. L. Marks, and D. R. Smith, "Design and simulation of a frequency diverse metamaterial aperture for imaging of human-scale targets," *IEEE Access*, vol. 4, pp. 5436-5451, 2016.

[4] O. Yurduseven, T. Fromenteze, C. Decroze, and V. Fusco, "Frequency-diverse computational automotive radar technique for debris detection," *IEEE Sens. J.*, vol. 20, no. 22, pp. 13167-13177, Nov. 2020.

[5] T. V. Hoang, R. Kumar, T. Fromenteze, M. G. Fernández, G. Á. Narciandi, V. Fusco, and O. Yurduseven, "Frequency selective computational through wall imaging using a dynamically reconfigurable metasurface aperture," *IEEE Open J. Antennas Propag.*, vol. 3, pp. 353-362, Apr. 2022.

[6] Z. Yang, G. Li, R. Yan, Y. Sun, L. Wu, and A. Zhang, "3-D computational ghost imaging with extended depth of field for measurement," *IEEE Trans. Instrum. Meas.*, vol. 68, no. 12, pp. 4906-4912, Dec. 2019.

[7] Y. Yu, J. Zheng, S. Chen, and Z. Yang, "Moving target imaging via computational ghost imaging combined with artificial bee colony optimization," *IEEE Trans. Instrum. Meas.*, vol. 71, Mar. 2021, Art. no. 4502107.

[8] Q. Wang, J. Mi, H. Shi, Z. Bai, L. Chen, H. Li, L. Zhang, and Y. Zhao, "Ghost imaging by single-layer neural network based based on forward physical model," *IEEE Trans. Instrum. Meas.*, vol. 73, Jul. 2023, Art. no. 4505310.

[9] M. F. Imani, J. N. Gollub, O. Yurduseven, A. V. Diebold, M. Boyarsky, T. Fromenteze, L. Pulido-Mancera, T. Sleasman, and D. R. Smith, "Review of metasurface antennas for computational microwave imaging," *IEEE Trans. Antennas Propag.*, vol. 68, no. 3, pp. 1860-1875, Mar. 2020.

[10] J. Hunt, T. Driscoll, A. Mrozack, G. Lipworth, M. Reynolds, D. Brady, and D. R. Smith, "Metamaterial apertures for computational imaging," *Science*, vol. 339, no. 6117, pp. 310-313, 2013.

[11] O. Yurduseven, M. F. Imani, H. Odabasi, J. Gollub, G. Lipworth, A. Rose, and D. R. Smith, "Resolution of the frequency diverse metamaterial aperture imager," *Prog. Electromagn. Res.*, vol. 150, pp. 97-107, 2015.

[12] M. Zhao, S. Zhu, J. Chen, X. Chen, and A. Zhang, "Broadband metamaterial aperture antenna for coincidence imaging in terahertz band," *IEEE Access*, vol. 8, pp. 121311-121318, Jul. 2020.

[13] J. Han, L. Li, S. Tian, X. Ma, Q. Feng, H. Liu, Y. Zhao, and G. Liao, "Frequency-diverse holographic metasurface antenna for near-field microwave computational imaging," *Front. Mater.*, vol. 8, Oct. 2021, Art. no. 766889.

[14] W. J. Padilla, and R. D. Averitt, "Imaging with metamaterials", *Nat. Rev. Phys.*, vol. 4, no. 2, pp.85-100, Feb. 2022.

[15] T. Sleasman, M. Boyarsky, L. Pulido-Mancera, T. Fromenteze, M. F. Imani, M. S. Reynolds, et al., "Experimental synthetic aperture radar with dynamic metasurfaces," *IEEE Trans. Antennas Propag.*, vol. 65, no. 12, pp. 6864-6877, Dec. 2017.

[16] M. F. Imani, T. Sleasman, and D. R. Smith, "Two-dimensional dynamic metasurface apertures for computational microwave imaging," *IEEE Antennas Wirel. Propag. Lett.*, vol. 17, pp. 2299-2303, Dec. 2018.

[17] J. Han, L. Li, S. Tian, G. Liu and Y. Shi, "Millimeter-wave imaging using 1-bit programmable metasurface: simulation model, design, and experiment," *IEEE J. Em. Sel. Top. C.*, vol. 10, pp.52-61, Mar. 2020.

[18] T. Zhou, H. Li, K. Xu, Q. Lv, and T. A. Denidni, "Experimental investigation on subwavelength imaging with temporal-spatial random illuminations," *IEEE Trans. Instrum. Meas.*, vol. 69, no. 1, pp. 18-20, Jan. 2021.

[19] C. Saigre-Tardif, R. Faqiri, H. Zhao, L. Li, and P. de Hougne, "Intelligent meta-imagers: From compressed to learned sensing," *Appl. Phys. Rev.*, vol. 9, no. 1, Mar. 2022, Art. no. 011314.

[20] T. Fromenteze, O. Yurduseven, M. Boyarsky, J. Gollub, D. L. Marks, and D. R. Smith, "Computational polarimetric microwave imaging," *Opt. Express*, vol. 25, no. 22, pp. 27488-27505, Oct. 2017.

[21] R. Peng, O. Yurduseven, T. Fromenteze, and D. R. Smith, "Advanced processing of 3D computational polarimetry using a near-field frequency-diverse antenna," *IEEE Access*, vol. 8, pp. 166261-166272, Sept. 2020.

[22] T. V. Hoang, V. Fusco, T. Fromenteze, and O. Yurduseven, " Computational polarimetric imaging using two-dimensional dynamic metasurface apertures," *IEEE Open J. Antennas Propag.*, vol. 2, pp. 488-497, Apr. 2021.

[23] M. Zhao, S. Zhu, H. Huang, D. Hu, X. Chen, J. Chen, and A. Zhang, "Frequency-diverse metamaterial cavity antenna for microwave coincidence imaging," *IEEE Antennas Wirel. Propag. Lett.*, vol. 20, no. 6, pp. 1103-1107, Apr. 2021.

[24] Y. Jiao, L. T. Lau, H. Hatzikirou, M. Meyer-Hermann, J. C. Corbo, and S. Torquato, "Avian photoreceptor patterns represent a disordered hyperuniform solution to a multiscale packing problem," *Phys. Rev. E*, vol. 89, Feb. 2014, Art. no. 022721.

[25] O. Christogeorgos, H. Zhang, Q. Cheng and Y. Hao, "Extraordinary directive emission and scanning from an array of radiation sources with hyperuniform disorder," *Phys. Rev. Appl.*, vol 15, Jan. 2021, Art. no. 014062.

[26] H. Zhang, Q. Cheng, H. Chu, O. Christogeorgos, W. Wu, and Y. Hao, "Hyperuniform disordered distribution metasurface for scattering reduction," *Appl. Phys. Lett.*, vol. 118, Mar. 2021, Art. no. 101601.

[27] J. Li, X. Wang, and T. Wang, "On the validity of born approximation," *Prog. Electromagn. Res.*, vol. 107, pp. 219-237, 2010.

[28] G. Lipworth, A. Mrozack, J. Hunt, D. R. Marks, T. Driscoll, D. Brady, and D. R. Smith, "Metamaterial apertures for coherent computational imaging on the physical layer," *J. Opt. Soc. Am. A*, vol. 30, no. 8, pp. 1603-1612, Aug. 2013.

[29] G. Lipworth, A. Rose, O. Yurduseven, V. R. Gowda, M. F. Imani, H. Odabasi, P. Trofatter, J. Gollub, and D. R. Smith, "Comprehensive simulation platform for a metamaterial imaging system," *Appl. Opt.*, vol. 54, no. 31, pp. 9343-9353, Oct. 2015.

[30] O. Yurduseven, T. Fromenteze, and D. R. Smith, "Relaxation of alignment errors and phase calibration in computational frequency-diverse imaging using phase retrieval," *IEEE Access*, vol. 6, pp. 14884-14894, Mar. 2018.

[31] T. V. Hoang, T. Fromenteze, M. A. B. Abbasi, C. Decroze, M. Khalily, V. Fusco, and O. Yurduseven, "Spatial diversity improvement in frequency-diverse computational imaging with a multi-port antenna," *Results Phys.*, vol. 22, Mar. 2021, Art. no. 103906.

[32] M. Zhao, S. Zhu, H. Huang, D. Hu, X. Chen, J. Chen, and A. Zhang, "W-band frequency-polarization-port-diverse cavity imager with bunching random beams," *J. Phys. D: Appl. Phys.*, vol. 54, no. 35, Sept. 2021, Art. no. 355106.

[33] O. Yurduseven, P. Flowers, S. Ye, D. L. Marks, J. N. Gollub, T. Fromenteze, B. J. Wiley, and D. R. Smith, "Computational microwave imaging using 3D printed conductive polymer frequency-diverse metasurface antenna," *IET Microw. Antennas Propag.*, vol. 11, no. 14, pp. 1962-1969, Nov. 2017.

[34] M. Zhao, S. Zhu, J. Li, H. Shi, J. Chen, Y. He and A. Zhang, "Frequency-diverse bunching metamaterial antenna for coincidence imaging," *Materials*, vol. 12, no. 11, Jun. 2019, Art. no. 1817.

[35] H. Zhang, W. Wu, Q. Cheng, Q. Chen, Y. Yu, and D. Fang, "Reconfigurable reflectarray antenna based on hyperuniform disordered distribution," *IEEE Trans. Antennas Propag.*, vol. 65, no. 7, pp. 7513-7523, Sept. 2022.

[36] B. Wu, X. Sheng, and Y. Hao, "Effective media properties of hyperuniform disordered composite materials," *PLos one*, vol. 12, no. 10, Oct. 2017, Art. no. e0185921.

[37] S. Torquato and F. H. Stillinger, "Local density fluctuations, hyperuniformity, and order metrics," *Phys. Rev. E*, vol. 68, Dec. 2003, Art. no. 041113.

[38] Y. Fan and J. K. Percus, "Constraints on collective density variables: One dimension," *Phys. Rev. A*, vol. 44, no. 4, pp. 2394-2401, Aug. 1991.

[39] O. U. Uche, F. H. Stillinger, and S. Torquato, "Constraints on collective density variables: Two dimension," *Phys. Rev. E*, vol. 70, Oct. 2004, Art. no. 046122.

[40] O. U. Uche, S. Torquato, and F. H. Stillinge, "Collective coordinate control of density distributions," *Phys. Rev. E*, vol. 74, Sept. 2006, Art. no. 031104.

[41] A. M. Molaei, T. Fromenteze, V. Skouroliakou, T. V. Hoang, R. Kumar, V. Fusco, and O, Yurduseven, "Development of fast fourier-compatible image reconstruction for 2D near-field bistatic microwave imaging with dynamic metasurface antennas," *IEEE Trans. Veh. Technol.*, vol. 71, no. 12, Dec. 2022.

[42] V. Skouroliakou, A. M. Molaei, M. G. Fernández, G. Á. Narciandi, and O. Yurduseven, "Frequency domain image reconstruction for imaging with multistatic dynamic metasurface antennas," *IEEE Access*, vol. 10, pp. 124728-124737, Nov. 2022.

[43] A. C. T. Yoya, B. Funchs, and M. Davy, "Computational passive imaging of thermal sources with a leaky chaotic cavity," *Appl. Phys. Lett.*, vol. 111, Nov. 2017, Art. no. 193501.
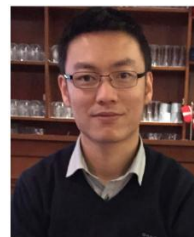
Mengran Zhao (Member, IEEE) received the B.S. degree in Information Engineering in 2016 and the Ph.D. degree in Electronic Science and Technology in 2021 from Xi'an Jiaotong University, Xi'an, China.

From 2018 to 2021, he was a Research Assistant with the School of Information and Communication Engineering, Xi'an Jiaotong University. Since 2022, he has been a Research Fellow with the Institute of Electronics, Communication and Information Technology (ECIT), Queen's University Belfast. He has published more than 30 papers. His research interests include metamaterial theory, computational imaging, chaotic cavity-based antenna design and multifunctional metasurface applications.

Shitao Zhu received the B.S. degree in electronic information science and technology from Lanzhou University, Lanzhou, China, in 2005, and the M.Sc. degree in information and communication engineering and the Ph.D. degree in electronic science and technology from Xi'an Jiaotong University, Xi'an, China, in 2008 and 2016, respectively.

From 2008 to 2012, he was a Systems Engineer with the ZTE Corporation, Ltd., Xi'an. He is currently an Associate Research Fellow with the School of Information and Communications Engineering, Xi'an Jiaotong University. His research interests include the metamaterial antenna, radar signal processing, and microwave coincidence imaging.

Xiaoming Chen (Senior Member, IEEE) received the B.Sc. degree in electrical engineering from Northwestern Polytech-nical University, Xi'an, China, in 2006, and the M.Sc. and Ph.D. degrees in electrical engineering from the Chalmers University of Technology, Gothenburg, Sweden, in 2007 and 2012, respectively.

From 2013 to 2014, he was a Post-Doctoral Researcher with the Chalmers University of Technology. From 2014 to 2017, he was with Qamcom Research and Technology AB, Gothenburg, Sweden. Since 2017, he has been a Professor with Xi'an Jiaotong University, Xi'an. His research areas include MIMO antennas, over-the-air (OTA) testing, reverberation chambers, and electromagnetic information theory.

Prof. Chen received the Outstanding AE Awards six times in 2017-2023. He also received the URSI (International Union of Radio Science) Young Scientist Awards in 2017 and 2018. He serves as an Associate Editor for IEEE Transactions on Antennas and Propagation and a Track Editor for IEEE Antennas and Wireless Propagation Letters.

Thomas Fromenteze received the Ph.D. degree from the University of Limoges, Limoges, France, in 2015.

From 2015 to 2016, he was a Postdoctoral Researcher with Duke University, Durham, NC, USA. He is currently a Maître de Conférences (Assistant Professor) with the Xlim Research Institute, University of Limoges. He is also an Adjunct Assistant Professor with the Center for Metamaterials and Integrated Plasmonics, Duke University. His research interests include ultra-wideband microwave and millimetre-wave imaging, wave propagation in complex media, computational/compressive imaging, and the various associated inverse problems. He was the recipient of the 11th EuRAD Young Engineer Prize during the European Microwave Week 2015.

Qammer H. Abbasi (Senior Member, IEEE) is a Professor with the James Watt School of Engineering (JWS), University of Glasgow, Glasgow, U.K., the Deputy Head of the Communication Sensing and Imaging Hub, the Lead of connecting people theme at JWS, and the Deputy Theme Lead of quantum technology with the University's Advance Research Centre. He has a grant portfolio of $10M+ and has published more than 450 journal articles and conference papers and edited/published 11 books.

Akram Alomainy (Senior Member, IEEE) is currently the Deputy Dean of Postgraduate Research with the Faculty of Science and Engineering, the Head of the Antennas and Electromagnetics Research Group, and a Reader in antennas and applied EM with the Queen Mary University of London (QMUL). He is also the Lead of Wearable Technology and Creativity Research. Research portfolio ranging from the basics of antennas and electromagnetism to novel applications in telerobotics, cognitive radio, wearable electronics, nano-scale networks, healthcare, and bioenigneering. He has over 450 publications in leading journals and international conferences (more than 10000 citations and H-index of 46). He is also a member of the Centre for Intelligent Sensing and Institute of Bioengineering. He is also a Chartered Engineer of IEEE and a member of IET.

He was a recipient of the 2011 British Science Festival Isambard Kingdom Brunel Award and a recipient of the QMUL Education Excellence Award, in 2019. He is also an Associate Editor of IEEE Antennas and Wireless Propagation Letters and IEEE Journal of Electromagnetics, RFand Microwaves in Medicine and Biology.

Vincent Fusco (Fellow, IEEE) is currently the Director of Research of the ECIT Research Institute, Queen's University Belfast, Belfast, U.K. His fundamental work on active antenna front-end techniques has provided generic advances in low-cost phased and self-tracking antenna array architectures. He has authored or coauthored more than 500 papers and two books. He holds a number of antenna-related patents.

Prof. Fusco is a Fellow of the Institution of Engineering and Technology and the Royal Academy of Engineering. He was the recipient of the IET Senior Achievement Award and Mountbatten Medal for seminal contributions in the field of microwave electronics and its impact on U.K. industry in 2012 and the 2019 Royal Irish Academy Gold medal for Engineering Science.

Okan Yurduseven (Senior Member, IEEE) received the Ph.D. degree in electrical engineering from Northumbria University, Newcastle upon Tyne, United Kingdom in 2014.

He is currently a Reader (Associate Professor) at the School of Electronics, Electrical Engineering and Computer Science, Queen's University Belfast, UK. Between 2018-2019, he was a NASA Research Fellow at the Jet Propulsion Laboratory, California Institute of Technology, USA. From 2014 to 2018, he was a Postdoctoral Research Associate at Duke University, USA.

His research interests include microwave and mm-wave imaging, multiple-input-multiple-output (MIMO) radars, wireless power transfer system, antennas and propagation, and metamaterials. He has authored more than 200 peer-reviewed technical journal and conference articles. He has secured, as Principal Investigator, research funding more than £3M and been the Co-Investigator on research grants in excess of £15M in these fields.

Dr Yurduseven is the recipient of several awards, including an Outstanding Postdoc at Duke University Award (2017), Duke University Professional Development Award (2017), NASA Postdoctoral Program Award (2018), British Council - Alliance Hubert Curien Award (2019), Leverhulme Trust Research Leadership Award (2020, £1M), Young Scientist Award from the Electromagnetics Academy - Photonics and Electromagnetics Research Symposium (2021), Queen's University Belfast Vice Chancellor's Early Career Researcher Prize (2022), and an Outstanding Associate Editor Award from the IEEE Antennas and Wireless Propagation Letters (2023). He serves as an Associate Editor of the IEEE Antennas and Wireless Propagation Letters and Nature Scientific Reports, and is a member of the European Association on Antennas and Propagation (EurAAP).